

This is the peer reviewed version of the following article: Lee, J., Song, H., Min, K. A., Guo, Q., Kim, D., Zheng, Z., ... & Lee, L. Y. S. (2021). Laser - Ablated Red Phosphorus on Carbon Nanotube Film for Accelerating Polysulfide Conversion toward High - Performance and Flexible Lithium–Sulfur Batteries. *Small Methods*, 5(7), 2100215, which has been published in final form at <https://doi.org/10.1002/smt.202100215>. This article may be used for non-commercial purposes in accordance with Wiley Terms and Conditions for Use of Self-Archived Versions.

DOI: 10.1002/ ((please add manuscript number))

**Article type: Full Paper**

## **Laser-ablated Red Phosphorus on Carbon Nanotube Film for Accelerating Polysulfide Conversion towards High-Performance and Flexible Lithium–Sulfur Batteries**

*Jeongyeon Lee, Hyeonjun Song, Kyung-Ah Min, Qianyi Guo, Daekyu Kim, Zijian Zheng, Byungchan Han,\* Youngjin Jung,\* Lawrence Yoon Suk Lee\**

Dr. Jeongyeon Lee; Daekyu Kim; Prof. Lawrence Yoon Suk Lee  
Department of Applied Biology and Chemical Technology, Research Institute for Smart Energy, The State Key Laboratory of Chemical Biology and Drug Discovery, The Hong Kong Polytechnic University, Hung Hom, Kowloon, Hong Kong SAR, China

Dr. Qianyi Guo; Prof. Zijian Zheng  
Laboratory for Advanced Interface and Materials, Research Centre for Smart Wearable Technology, Institute of Textiles Clothing, The Hong Kong Polytechnic University, Hung Hom, Hong Kong SAR, China

Hyunjun Song; Prof. Youngjin Jung  
Department of Organic Materials and Fiber Engineering, Soongsil University, Seoul 156-743, Republic of Korea

Dr. Kyung-Ah Min; Prof. Byungchan Han  
Department of Chemical & Biomolecular Engineering, Yonsei University, Seoul 03722, Republic of Korea

E-mails: *bchan@yonsei.ac.kr; yjeong@ssu.ac.kr; lawrence.ys.lee@polyu.edu.hk*

**Keywords:** *interlayer; red phosphorus; pulsed laser ablation; Li–S battery; morphologic effect*

The use of a conducting interlayer between separator and cathode is one of the most promising methods to trap lithium polysulfides (LiPSs) for enhancing the performance of lithium–sulfur (Li–S) batteries. We report herein red phosphorus nanoparticles (RP<sub>EN</sub>)-coated carbon nanotube (CNT) film (RP<sub>EN</sub>@CF) as a novel interlayer for Li–S batteries, which shows strong chemisorption of LiPSs, good flexibility, and excellent electric conductivity. A pulsed laser ablation method is engaged for the ultrafast production of RP<sub>EN</sub> of uniform morphology, which are deposited on the CNT film by a direct spinning method. The RP<sub>EN</sub>@CF interlayer provides

pathways for effective  $\text{Li}^+$  and electron transfer and strong chemical interaction with LiPSs. The  $\text{S/RP}_{\text{EN}}@\text{CF}$  electrode shows a superior specific capacity of  $782.3 \text{ mA h g}^{-1}$  (3 C-rate) and good cycling performances ( $769.5 \text{ mA h g}^{-1}$  after 500 cycles at 1 C-rate). Density functional theory calculations reveal that the morphology and dispersibility of  $\text{RP}_{\text{EN}}$  are crucial in enhancing  $\text{Li}^+$  and electron transfer kinetics and effective trap of LiPSs. This work demonstrates the possibility of using the  $\text{RP}_{\text{EN}}@\text{CF}$  interlayer for the enhanced electrochemical performances of Li–S batteries and other flexible energy storage devices.

## 1. Introduction

Lithium–sulfur (Li–S) batteries, having the advantages of cost-effectiveness and high theoretical capacity ( $1,675 \text{ mA h g}^{-1}$ ), are considered as one of the most promising candidates for large-scale energy storage devices such as electric vehicles and energy storage systems.<sup>[1]</sup> The commercialization of Li–S batteries is, however, still hindered by low utilization and large volume change of S, as well as the shuttle effect of lithium polysulfides (LiPSs) during the charge/discharge cycles.<sup>[2]</sup> In particular, the repeated redox reactions of soluble LiPSs at the anode and cathode continuously consume the active S cathode and electrons as a result of the shuttle mechanism, causing capacity fading and low energy efficiency of Li–S batteries.<sup>[3]</sup>

Initial approaches to minimize the dissolution and diffusion of LiPSs involved the trapping of LiPSs by various carbonaceous materials, such as porous carbon materials,<sup>[4]</sup> carbon nanotubes (CNTs),<sup>[5]</sup> and graphene,<sup>[6]</sup> to impregnate the elemental S. To mitigate the shuttle effect by strong chemical adsorption, various carbon composites containing catalytic materials, including metal oxides/sulfides,<sup>[7]</sup> conducting polymers,<sup>[8]</sup> and metal–organic frameworks (MOFs),<sup>[9]</sup> have been engaged as S cathode supports. Despite the improved electrochemical performances, most Li–S batteries still suffer from the continuous dissolution of LiPSs in the cathode side, especially during the long-term cycling. The use of highly porous carbon

composites and low S loading would effectively suppress the dissolution of LiPSs but at the cost of energy density. It is thus highly desirable to explore novel approaches that can suppress the shuttle effect while retaining the high S loading in the cathode.

Conducting interlayers made of carbon materials between the separator and cathode offer an alternative strategy to overcome these challenges. Such interlayers can play a role of direct physical barrier that reduces the diffusion of LiPSs while providing good electric conductivity and 3D channels for facilitated transport of electrons and Li ions.<sup>[10]</sup> However, it is difficult to fully suppress the shuttle effect by carbon-only interlayers owing to their weak physical interaction with the LiPSs, similar to the case of the cathodes designed with carbon materials only. For this reason, several metal oxides,<sup>[11]</sup> sulfides,<sup>[12]</sup> and nitrides<sup>[13]</sup> have been incorporated to the interlayer as a catalytic additive to induce the stronger chemical adsorption of LiPSs and thereby enhance the performance of Li–S batteries. Recently, phosphorus and phosphide-based materials, for examples, black phosphorus (BP),<sup>[14]</sup> red phosphorus (RP),<sup>[15]</sup> and CoP,<sup>[16]</sup> were shown to efficiently confine the LiPSs by strong chemical adsorption. Such multifunctional interlayers could enhance both rate capability and cyclic performances, as well as enable the construction of flexible electrodes. The challenge lies in the complicated preparation of conductive and catalytic interlayer, especially with the control of thickness, weight, and distribution of catalytic materials, which are crucial for minimizing the charge transfer resistance and capacity fading.

Herein, we designed a freestanding and flexible conducting interlayer for Li–S batteries based on RP nanoparticles (RP<sub>EN</sub>) coated on CNT film (RP<sub>EN</sub>@CF), which delivers a high energy density and fast LiPSs redox kinetics. The pulsed-laser ablation of bulk RP crystal (RP<sub>B</sub>) allowed its ultrafast and uniform exfoliation to RP<sub>EN</sub> of < 20 nm in size. The RP<sub>EN</sub> were homogeneously loaded on the CNT film that was synthesized by a direct spinning method. The RP<sub>EN</sub>@CF interlayer provides synergistic advantages of high electric conductivity and physical

barrier for LiPSs, which lead to the enhanced specific capacity and cycle stability in various electrochemical tests of assembled Li–S batteries. Based on experimental analyses and the first-principle density functional theory (DFT) calculations of  $\text{RP}_{\text{EN}}@\text{CF}$  and  $\text{RP}_{\text{B}}@\text{CF}$  interlayers, we demonstrate the impacts of RP morphology and dispersibility on the electrochemical performances and stability of Li–S batteries.

## 2. Results and Discussion

**Figure 1a** illustrates the procedure for fabricating carbon nanotube (CNT) film coated with red phosphorus (RP) nanoparticles that are produced using the laser-assisted exfoliation setup (**Figure S1**, the Supporting Information). The bulk red phosphorus ( $\text{RP}_{\text{B}}$ ) crystal in methanol is irradiated by an Nd:YAG Q-switched pulsed laser ( $\lambda = 1,064 \text{ nm}$ ,  $650 \text{ mJ}$ ) with a pulse width of  $80 \text{ ns s}^{-1}$  and a repetition rate of  $10 \text{ Hz}$  to yield exfoliated red phosphorus nanoparticles ( $\text{RP}_{\text{EN}}$ ) as an orange suspension. The transmission electron microscopic (TEM) image of  $\text{RP}_{\text{EN}}$  (**Figure 1b**) shows considerable size reduction compared with  $\text{RP}_{\text{B}}$  (**Figure S2**), despite the partial aggregation due to electrostatic interaction. Dynamic light scattering (DLS) analysis indicates that the diameter of the  $\text{RP}_{\text{EN}}$  ranges from  $10$  to  $20 \text{ nm}$  with an average diameter of  $15 \text{ nm}$  (inset in **Figure 1b**). As a suitable substrate for loading the as-prepared  $\text{RP}_{\text{EN}}$  as well as a conducting interlayer for Li–S batteries, a light and flexible CNT film was synthesized by a direct spinning method.<sup>[17]</sup> The structural characteristics of the CNT film was first analyzed by Raman spectroscopy (**Figure S3a**). The G/D ratio, calculated by dividing the peak area of G-band ( $1,580 \text{ cm}^{-1}$ ) with that of D-band ( $1,360 \text{ cm}^{-1}$ ), is related to the crystalline perfection of CNTs. A high G/D ratio of  $6.73$  indicates that the CNT film has a high crystallinity with few defects.<sup>[18]</sup> The XPS analysis of CNT film reveals that the surface concentration of oxygen-containing functional groups (C–O and O–C=O) is low (**Figure S3b**), which supports small number of defects.<sup>[19]</sup> The Raman and XPS results imply that the CNT film synthesized *via* the

direct spinning method has high crystallinity that would endow enhanced durability. The nitrogen adsorption–desorption isotherm of the CNT film (**Figure S3c**) shows a surface area of  $175.51 \text{ m}^2 \text{ g}^{-1}$  with a typical hysteresis of mesoporous structure<sup>[20]</sup> that is advantageous for retaining good wettability of electrolyte and fast  $\text{Li}^+$  transport. The mechanical strength of the CNT film was evaluated as shown in **Figure S3d**. The CNT film exhibits 4.5 GPa of high tensile strength, which is considerable higher than that of the bucky CNT paper fabricated by vacuum filtration of a CNT-dispersed solution. Such an outstanding mechanical strength of the CNT film can be explained by its network structure in which individual CNT bundles of high aspect ratio are entangled one another. The scanning electron microscopic (SEM) images (**Figures S4**) show that such interwoven network structure is absent in the bucky paper.

To fabricate the  $\text{RP}_{\text{EN}}$ -coated CNT film ( $\text{RP}_{\text{EN}}@\text{CF}$ ) as a conducting interlayer having strong chemical interaction with LiPSs, the methanolic solution of the as-prepared  $\text{RP}_{\text{EN}}$  (0.1 mL,  $2 \text{ mg mL}^{-1}$ ) was drop-cast onto a circular CNT film ( $d = 14 \text{ mm}$ ) and heated on a hotplate at  $70^\circ \text{C}$  to evaporate the solvent in an Ar-filled glovebox. The surface of  $\text{RP}_{\text{EN}}@\text{CF}$  shows a uniform distribution of  $\text{RP}_{\text{EN}}$  as evidenced by SEM image and the corresponding energy-dispersive X-ray spectra (EDS) elemental mapping images of P and C (**Figure S5**). On the contrary, the control sample prepared with  $\text{RP}_{\text{B}}$  using the same protocol ( $\text{RP}_{\text{B}}@\text{CF}$ ) exhibits uneven distribution of  $\text{RP}_{\text{B}}$  (**Figure S6**). Both interlayers have the good flexibility and lightweight (*ca.* 2.2 mg). To further confirm the morphology of  $\text{RP}_{\text{EN}}@\text{CF}$ , TEM analysis was conducted by loading the  $\text{RP}_{\text{EN}}@\text{CF}$  sonicated in methanol onto a TEM grid. Despite the partial detachment of  $\text{RP}_{\text{EN}}$  from CNT film during the sonication process, majority of  $\text{RP}_{\text{EN}}$  remains well-attached on CNT film (**Figures 1c** and **1d**). The high-resolution TEM shown as the inset in **Figure 1d** indicates the amorphous phase of  $\text{RP}_{\text{EN}}$ , and EDS mapping in **Figure 1e** confirms the presence of elemental P and C.

**Figure 2a** shows the digital images of the CNT film, RP<sub>EN</sub>@CF, and RP<sub>B</sub>@CF interlayers. The actual amounts of RP nanoparticles loaded on the CNT film were determined by TGA analysis (**Figure 2b**). Despite the higher decomposition temperature of RP<sub>B</sub> owing to its larger particle size, both RP<sub>B</sub> and RP<sub>EN</sub> display the similar weight loss of about 28 wt.% at > 550 °C. **Figure 2c** compares the X-ray diffraction (XRD) patterns of RP<sub>B</sub>@CF and RP<sub>EN</sub>@CF. The RP<sub>B</sub> exhibits typical diffraction peaks at 15°, 34°, and 55°, indicating a medium-range ordered structure,<sup>[21]</sup> while RP<sub>EN</sub> displays very weak peaks that appear as amorphous phase due to their small size. Raman spectrum of RP<sub>EN</sub> reveals three distinguished peaks at 355.9, 385.0, 455.2 cm<sup>-1</sup> corresponding to the B<sub>1</sub>, A<sub>1</sub>, and E<sub>1</sub> modes of RP (**Figure 1d**).<sup>[21]</sup> The Raman peaks of RP<sub>EN</sub> are initially much stronger than those of RP<sub>B</sub> (**Figure S7**), but diminish with the time exposed to air and almost disappear after 6 h. The microscopic images of RP<sub>EN</sub> shown in **Figure S8** confirm the gradual increase of the oxidized area on RP<sub>EN</sub> surface with the exposure time in air.

The surface chemical states and compositions of the as-prepared samples were investigated by X-ray photoelectron spectroscopy (XPS), as shown in **Figures 2e, 2f, and S9**. The survey XPS spectrum of the RP<sub>EN</sub>@CF confirms the existence of C and P elements (**Figure S9a**). The high-resolution XPS spectra of RP<sub>EN</sub>@CF and RP<sub>B</sub>@CF in C 1s region can be deconvoluted to three peaks centered at 284.4, 285.4, and 289.9 eV, which correspond to C=C/C–C (sp<sup>2</sup>), C–C (sp<sup>3</sup>), and P–C=O/O–C=O, respectively (**Figures 2e and S9b**).<sup>[22]</sup> The O 1s peak in the survey spectrum originates from the inevitable surface oxidation of RP during the pulsed-laser ablation in methanol, forming H<sub>m</sub>PO<sub>n</sub> by the interaction with O<sub>2</sub>.<sup>[23]</sup> The TEM EDS mappings of RP<sub>EN</sub>@CF and RP<sub>B</sub>@CF also reveal O atoms (**Figure S10**), which support the surface oxidation of both RP samples in an oxygen-containing atmosphere. The chemical bonding between RP and carbon in both RP<sub>EN</sub>@CF and RP<sub>B</sub>@CF is also evidenced by the characteristic P–O–C peak at 134.1 eV in P 2p region (**Figures 2f**).<sup>[24]</sup> The RP<sub>EN</sub>@CF shows the more distinct

P–O–C and P–O peaks (135.1 eV) due to the more severe surface oxidation of much smaller  $\text{RP}_{\text{EN}}$  compared with  $\text{RP}_{\text{B}}$ . To confirm the surface oxidation states, P–O–C peaks in P 2p XPS spectra of  $\text{RP}_{\text{EN}}@\text{CF}$  and  $\text{RP}_{\text{B}}@\text{CF}$  are compared in **Figure S9**, which implies that the  $\text{RP}_{\text{EN}}$  in  $\text{RP}_{\text{EN}}@\text{CF}$  has a much higher surface area than  $\text{RP}_{\text{B}}$ , resulting in the better dispersibility of  $\text{RP}_{\text{EN}}$  on CNT film. The P 2p XPS spectra of  $\text{RP}_{\text{EN}}@\text{CF}$  and  $\text{RP}_{\text{B}}@\text{CF}$  also display two deconvoluted peaks at 130.1 and 131.0 eV, which are assigned to P 2p<sub>1/2</sub> and P 2p<sub>3/2</sub> states, respectively.<sup>[24a]</sup>

To investigate the effect of  $\text{RP}_{\text{EN}}@\text{CF}$  interlayer on the electrochemical performance of Li–S battery, typical S-infiltrated Super P ( $\text{S}@\text{Super P}$ ) was used as a sulfur cathode with the  $\text{RP}@\text{CF}$ s inserted as interlayers (denoted as  $\text{S}/\text{RP}_{\text{EN}}@\text{CF}$  and  $\text{S}/\text{RP}_{\text{B}}@\text{CF}$ ). As a control sample,  $\text{S}@\text{Super P}$  with bare CNT film interlayer ( $\text{S}/\text{CF}$ ) was also prepared. Based on the TGA analysis under  $\text{N}_2$  atmosphere, the actual sulfur content in total weight of  $\text{S}@\text{Super P}$  is determined as 75.6 wt.% (**Figure S11**). Cyclic voltammetry (CV) was first conducted using the  $\text{S}/\text{RP}@\text{CF}$  and  $\text{S}/\text{CF}$  electrodes (**Figures 3a** and **S12**) in the potential window between 1.7 and 2.8 V at a scan rate of 0.1 mV s<sup>−1</sup>. Typical two reduction peaks (2.31 and 2.05 V) and two oxidation peaks (2.30 and 2.36 V) are observed from the CV of  $\text{S}/\text{RP}_{\text{EN}}@\text{CF}$ , which correspond to the reversible redox reactions of S to  $\text{Li}_2\text{S}_2/\text{Li}_2\text{S}$ .<sup>[25]</sup> Compared with  $\text{S}/\text{CF}$  electrode,  $\text{S}/\text{RP}_{\text{EN}}@\text{CF}$  displays the higher peak currents accompanied by remarkable shifts of cathodic peaks (by 17 and 42 mV) and anodic peaks (by −49 mV). The  $\text{S}/\text{RP}_{\text{B}}@\text{CF}$  electrode shows similar redox peaks as  $\text{S}/\text{RP}_{\text{EN}}@\text{CF}$ , which are shifted slightly less. These results disclose that the polysulfide conversion kinetics of  $\text{S}/\text{CF}$  is improved by inserting the  $\text{RP}_{\text{EN}}@\text{CF}$  and  $\text{RP}_{\text{B}}@\text{CF}$  interlayers. **Figure 4b** shows the galvanostatic charge/discharge curves of  $\text{S}/\text{RP}_{\text{EN}}@\text{CF}$  at 0.1 C, which indicate the specific capacities of 1,202.8 and 1,218.7 mA h g<sup>−1</sup> in the first cycle, respectively. The overpotential between the charge and discharge curves at 500 mA h g<sup>−1</sup> is narrower for  $\text{S}/\text{RP}_{\text{EN}}@\text{CF}$  (ca. 0.142 V) compared with  $\text{S}/\text{RP}_{\text{B}}@\text{CF}$  (ca. 0.171

V, **Figure S13**), indicating the lower polarization of S/RP<sub>EN</sub>@CF owing to the more efficient catalytic effect by RP<sub>EN</sub> that is homogeneously and densely loaded on the CNT film.

To further compare the catalytic capability, the Li<sup>+</sup> diffusivities of S/RP<sub>EN</sub>@CF and S/RP<sub>B</sub>@CF electrodes were calculated based on the CVs measured at various scan rates (**Figures 4c** and **S14**) using the Randles–Sevcik equation (1):<sup>[26]</sup>

$$I_p = (2.69 \times 10^5) n^{1.5} A D_{Li}^{0.5} C_{Li} v^{0.5} \quad (1)$$

where  $I_p$  is the peak current,  $n$  is the number of electrons transferred,  $A$  is the electrode surface area,  $D_{Li}$  is the diffusion coefficient for Li<sup>+</sup>,  $C_{Li}$  is the concentration of Li<sup>+</sup>, and  $v$  is the scan rate. According to the variation of cathodic and anodic peak positions in the CVs, the  $D_{Li}$  values are calculated from the linear relationship of  $I_p$  vs.  $v^{0.5}$ . The S/RP<sub>EN</sub>@CF electrode exhibits the steeper slopes for both cathodic and anodic peaks (C1: −373 and A1: 576, **Figure S15**) compared with the S/RP<sub>B</sub>@CF (C1: −331 and A1: 443), which clearly indicates the faster redox kinetics of S/RP<sub>EN</sub>@CF.

The synergistic effect of inserting a conductive CNT film interlayer loaded with RP<sub>EN</sub> catalysts on Li–S battery performances was investigated by conducting various electrochemical tests. In this work, the S@Super P electrode (75.6 wt.% of S loading) was used as a standard sulfur cathode for all electrochemical tests. **Figure S16** shows the cycling performance of bare S@Super P electrode at 1.0 C-rate for 500 cycles, where low specific capacity and severe capacity fading are evident. The cycling test was also conducted with only CNT film as an active material under the same conditions to examine the contribution of CNT film to the capacity. As shown in **Figure S17**, CNT film electrode exhibits a negligible capacity (< 1 mA h g<sup>−1</sup>) because of unmatched potential window, which confirms no contribution of CNT film to capacity. The rate capabilities of S/RP<sub>EN</sub>@CF, S/RP<sub>B</sub>@CF, and S/CF cells are compared in **Figure 4d**. The S/RP<sub>EN</sub>@CF electrode maintains the higher capacity values at various C-rates compared with other electrodes. At 3 C-rate, both S/RP@CF cells show much better



performances than S/CF electrode. In particular, the S/RP<sub>EN</sub>@CF achieves the highest capacity of 782.3 mA h g<sup>-1</sup>. In the cycling tests (**Figure 4e**), the S/RP<sub>EN</sub>@CF electrode retains a specific capacity of 889.5 mA h g<sup>-1</sup> at the end of 200 cycles, delivering remarkably stable and higher cycle performance compared with S/RP<sub>B</sub>@CF and S/CF cells. Cycling performance and the stability with high S loading are crucial for commercialization of Li-S batteries. **Figure 4f** presents the cycling performances of S/RP<sub>EN</sub>@CF electrodes with higher S loadings tested at 0.2 C-rate for 100 cycles. The S/RP<sub>EN</sub>@CF electrodes with S loadings of 3.8, 5.0, and 6.3 mg (75 wt.% S content) show high areal capacities of 2.47, 2.52, and 3.63 mA h cm<sup>-2</sup> over 100 cycles, respectively. Such excellent cycle performances and stability of S/RP<sub>EN</sub>@CF electrodes, even with the basic sulfur cathode (S@Super P) of limited electrochemical performance, can be ascribed to the synergistic effect of RP<sub>EN</sub>@CF that played both catalytic and physical roles in reducing the diffusion of LiPSs. Another critical parameter for commercialization of Li-S battery is the long-term cycling stability, which was tested at 1.0 C-rate for 500 cycles (**Figure 4g**). An initial specific capacity of 1,050.2 mA h g<sup>-1</sup> is measured from S/RP<sub>EN</sub>@CF electrode and it slowly decreases in the following cycles and retains 769.5 mA h g<sup>-1</sup> at the end of 500 cycles. In addition, S/RP<sub>EN</sub>@CF shows the coulombic efficiency > 99% during 500 cycles. This stable and high cycle performance reveals that RP<sub>EN</sub>@CF can effectively trap and activate the polysulfide conversion even for long-term cycles.

To gain an insight into the improved electrochemical performances of S/RP<sub>EN</sub>@CF, the first-principles density functional theory (DFT) calculations were carried out and the catalytic and morphological efficacies of RP@CF interlayers for the chemical interaction with LiPSs were examined (**Figure 4**). The chemical adsorption strengths of LiPSs on RP and CNT were evaluated over the charging and discharging process in the Li-S batteries. The adsorption energy ( $E_{\text{ads}}$ ) of Li<sub>2</sub>S<sub>x</sub> ( $x = 1, 2, 4, 6, \text{ and } 8$ ) was defined as Eq. (1):

$$E_{\text{ads}} = E_{\text{LiPS/RP(or CNT)}} - (E_{\text{LiPS}} + E_{\text{RP(or CNT)}}) \quad (1)$$

where  $E_{\text{LiPS/RP(or CNT)}}$  is total energy of LiPSs adsorbed on RP (or CNT), while  $E_{\text{LiPS}}$  and  $E_{\text{RP(or CNT)}}$  mean total energy of isolated LiPSs and RP (or CNT), respectively. Here, the more negative  $E_{\text{ads}}$  is, the stronger the adsorption strength of LiPSs would be. **Figure 4a** shows that LiPSs chemisorb more strongly at the top than edge sites of RP through Li–P bond formation. The adsorption strengths tend to decrease as the size of the LiPSs increases (**Figure 4a**), yet all the adsorption strengths are sufficient for chemical trap of the LiPSs.

The thermodynamic plausibility of long-chain polysulfide formation *via* the agglomeration between adsorbed LiPSs on RP was investigated by calculating the adsorption of two LiPSs on different sites in RP. It was identified that short-chain polysulfides such as  $\text{Li}_2\text{S}$  energetically prefer mutual agglomeration with each other (**Figures S18a and S18b**) at the top site of RP. On the contrary, long-chain polysulfides such as  $\text{Li}_2\text{S}_6$  are hardly agglomerated on the RP regardless of the adsorption sites (**Figures S19a and S19b**). This means that RP can effectively capture the LiPSs without growing them into long-chain polysulfides by agglomeration.

As shown in **Figure 4b**, our calculations indicate that LiPSs physisorb on CNT through van der Waals interaction, which is much weaker than the interaction with RP. This clearly indicates that RP can act as an effective chemical trapper of LiPSs, while CNT plays a role of a physical counterpart. As illustrated in **Figure 4c**,  $\text{RP}_{\text{EN}}$  nanoparticles are more uniformly distributed on CNT film than the  $\text{RP}_{\text{B}}$ . This does not mean that such a distribution of  $\text{RP}_{\text{EN}}$  is induced by strong chemical interaction with CNT, because the binding energies ( $E_{\text{b}}$ ) between RP and CNT do not significantly change with varying RP sizes (**Figures S20a and S20b**). Instead, the relatively smaller size of  $\text{RP}_{\text{EN}}$  enables the stronger adsorption on CNT compared with the  $\text{RP}_{\text{B}}$ . In other words, the larger surface area of RP is exposed in  $\text{S/RP}_{\text{EN}}@\text{CF}$  than  $\text{S/RP}_{\text{B}}@\text{CF}$ , leading to the effective trapping of LiPSs *via* the chemisorption process (**Figure 4c**). The morphological differences illustrated in **Figure 4c** can be visualized by the tilted-view SEM images of  $\text{RP}_{\text{B}}@\text{CF}$  and  $\text{RP}_{\text{EN}}@\text{CF}$  (**Figure S21**), which strongly support our explanation.

Furthermore, these tilted-view SEM images correspond to the P–O–C peaks in XPS spectra of  $\text{RP}_{\text{EN}}@\text{CF}$  (**Figure S9d**), which prove that the electrochemical performance of Li–S batteries considerably depends on the morphology and dispersibility of catalysts, as well as its intrinsic properties for confining and catalyzing the LiPSs. Therefore, the fine coverage of  $\text{RP}_{\text{EN}}$  catalysts for the LiPSs delivers the higher electrochemical performances of  $\text{S}/\text{RP}_{\text{EN}}@\text{CF}$  cells in Li–S batteries. To further understand the catalytic effect of  $\text{RP}_{\text{EN}}$  and  $\text{RP}_{\text{B}}$  toward LiPSs trapping, UV–vis adsorption tests were conducted (**Figure 5a**). With the addition of  $\text{RP}_{\text{EN}}$  and  $\text{RP}_{\text{B}}$  powders (10 mg), the color of 10 mM  $\text{Li}_2\text{S}_6$  solutions changes to almost colorless and pale yellow, respectively, and the characteristic  $\text{Li}_2\text{S}_6$  absorption peak at around 420 nm disappears after 24 h, which illustrate strong LiPSs adsorption abilities of both  $\text{RP}_{\text{EN}}$  and  $\text{RP}_{\text{B}}$ .

The impact of  $\text{RP}@\text{CF}$  on polysulfide conversion kinetics was investigated by engaging galvanostatic electrochemical impedance spectroscopy (GEIS) for both fresh and cycled cells (**Figures 5b** and **5c**). All Nyquist plots of  $\text{S}/\text{RP}_{\text{EN}}@\text{CF}$ ,  $\text{S}/\text{RP}_{\text{B}}@\text{CF}$ , and  $\text{S}/\text{CF}$  display similar features of a semicircle at high frequency domain and a diffusion line at the middle to low frequency domain. In fresh cells, the charge-transfer resistance ( $R_{\text{ct}}$ ) determined by the diameter of semicircle is the lowest for  $\text{S}/\text{RP}_{\text{EN}}@\text{CF}$  cell (31.0  $\Omega$ ) compared with the  $\text{S}/\text{RP}_{\text{B}}@\text{CF}$  (54.0  $\Omega$ ) and  $\text{S}/\text{CF}$  (81.5  $\Omega$ ) electrodes, which reveals the superior  $\text{Li}^+$  and electron transfer pathways of  $\text{S}/\text{RP}_{\text{EN}}@\text{CF}$  cell. The diffusion line of  $\text{S}/\text{RP}_{\text{B}}@\text{CF}$  cell is less steep compared with those of  $\text{S}/\text{RP}_{\text{EN}}@\text{CF}$  and  $\text{S}/\text{CF}$  cells, which could be affected by the slower diffusion rate due to larger size of  $\text{RP}_{\text{B}}$  and its poor distribution on CNT film. The GEIS results after 100 cycles also show the lowest  $R_{\text{ct}}$  for  $\text{S}/\text{RP}_{\text{EN}}@\text{CF}$  cell, confirming the effective confinement and catalytic conversion of polysulfides during the cycling. After 100 cycles, the diffusion line is the steepest for  $\text{S}/\text{RP}_{\text{EN}}@\text{CF}$  cell, followed by  $\text{S}/\text{RP}_{\text{B}}@\text{CF}$  and  $\text{S}/\text{CF}$ , which supports the importance of size and dispersibility of RP catalysts for the enhanced electrochemical performance.

The Li–S full cell was constructed using Li metal on NiCF, the RP<sub>EN</sub>@CF interlayer, and S@Super P on CuCF (2.77 mg of S loading) and its mechanical durability and cycle stability were evaluated by measuring the specific capacities during progressive mechanical roll-up (**Figure 5e**). The Li–S full cell was cycled at 0.1 C-rate for 100 h each with flat configuration and three roll-up radii of 15, 7.5, and 5 mm. The initial specific capacity measured with flat configuration (1177.8 mA h g<sup>-1</sup>) slightly fades to 896.6, 747.5, and 601.5 mA h g<sup>-1</sup> at the end of each roll-up cycles, which show the remarkable mechanical durability of Li–S full cell with minute fluctuations upon the external pressure. The light bulb connected to the Li–S full cell was maintained on during the entire mechanical roll-up process, which indicates good cycle stability and excellent flexibility of RP<sub>EN</sub>@CF interlayer.

### 3. Conclusion

In summary, an efficient RP<sub>EN</sub>@CF interlayer for Li–S batteries was successfully synthesized with the aid of pulsed laser ablation and direct spinning method. Owing to the uniform and nanosized morphology of RP<sub>EN</sub> and its strong chemisorption to LiPSs, the RP<sub>EN</sub>@CF interlayer demonstrates a high efficiency in suppressing the LiPS diffusion and enhances the electrochemical performance of Li–S battery with high Coulombic efficiency and long cycle stability. A high rate capability (782.3 mA h g<sup>-1</sup> at 3 C-rate) and stable cycling performances (769.5 mA h g<sup>-1</sup> at 1 C-rate) even after 500 cycles as well as the good cycle stability with rolled-up electrodes are delivered. DFT calculations results support the electrochemical data, demonstrating that RP<sub>EN</sub>@CF can effectively trap LiPSs by strong Lewis acid–base interaction. This novel RP<sub>EN</sub>@CF interlayer enables the enhanced electrochemical performances of Li–S batteries and shows the possibility of use in other flexible energy storage devices such as sodium-ion batteries and supercapacitors.

#### 4. Experimental Section

*Materials.* Acetone (99.7 %) was purchased from Samchun Chemical. Bulk red phosphorus (RP<sub>B</sub>), ferrocene (98 %), thiophene ( $\geq 99$  %), polysorbate 20, and methanol were purchased from Sigma–Aldrich. The RP<sub>B</sub> was hydrothermally treated to remove the surface oxide layer. Aluminum foil, *N*-methyl-2-pyrrolidone (NMP), conductive carbon black (TIMCAL graphite & carbon Super P), and polyvinylidene fluoride (PVDF, HSV900) were purchased from MTI. Electrolyte solution containing 1 M lithium bis(trifluoromethane) sulfonamide (LiTFSI) in the 1:1 mixed solvent of ethylene carbonate and diethyl carbonate was obtained from DodoChem.

*Pulsed laser-assisted exfoliation of RP.* A Nd:YAG Q-switched pulsed laser (Nimma-600 Laser system) with an energy output of 650 mJ and energy stability (RMS)  $\leq 1\%$  was purchased from Beamtech Optronics Co.Ltd. The diameter of beam is *ca.* 8 mm and the distance between the RP<sub>B</sub> and the liquid surface is 2 cm. Before laser treatment, the solvent containing RP<sub>B</sub> was purged by bubbling Ar gas to prevent oxidation.

*Fabrication of flexible CNT film.* Flexible CNT film was prepared by a direct spinning method following a previous report.<sup>[17]</sup> Briefly, a precursor solution containing acetone (93 wt.%, carbon source), ferrocene (1.2 wt.%, catalyst precursor), thiophene (4.8 wt.%, promoter), and polysorbate 20 (1 wt.%, surfactant) was injected (11 mL h<sup>-1</sup>) into a vertical furnace (1200 °C) with a H<sub>2</sub> gas flow (1100 sccm, carrier gas) to synthesize a CNT sock. The synthesized CNT sock was collected by rotating winder at the bottom of the vertical furnace to fabricate a flexible CNT film.

*Sulfur-infiltrated Super P (S@Super P).* Sulfur and Super P were mixed in a mortar with a weight ratio of 3:1 for 1 h. The sulfur was infiltrated into Super P *via* a typical melt-diffusion method by heating the as-prepared mixture at 155 °C for 16 h in a tube furnace under a gentle flow of Ar gas.

*Li<sub>2</sub>S<sub>6</sub> solution.* A Li<sub>2</sub>S<sub>6</sub> solution (10 mM) was prepared by dissolving sulfur and Li<sub>2</sub>S with a molar ratio of 5:1 in a mixed solvent (1:1 volume ratio) of 1,3-dioxolane and 1,2-dimethoxyethane under vigorous stirring at 60 °C for 24 h in a glovebox.

*Material characterizations.* TEM analysis and EDX mapping were conducted on a JEOL system (Model JEM-2100F, 200 kV). For the TEM sample preparation, a sonicated solution of RP<sub>EN</sub>@CF was drop-cast on a Ni grid. SEM analysis was performed on a TESCAN MAIA3 system. XPS spectra were collected using a Thermo Fisher ESCALAB 250Xi system. The spectrometer was calibrated with the C 1s peak at 284.6 eV. XPS 41 software was used for data fitting. UV–vis spectroscopy was performed using an AvaLight UV/vis/NIR light source with an AvaSpex-UL S2048 Fiber-Optic spectrometer. Raman spectra were acquired from a Witec confocal Raman system (alpha300 R). The excitation laser ( $\lambda = 532$  nm) of 5 mW energy was used for all tests to minimize sample burning. X-ray diffraction (XRD) patterns were collected using a SmartLab X-ray diffractometer by Rigaku (voltage 45 kV, current 200 mA). Thermogravimetric analysis (TGA) was conducted on a thermal analyzer (TGA/DSC 1, Mettler Toledo Co.) at a heating rate of 10 °C min<sup>-1</sup> in N<sub>2</sub>/air gas.

*Battery cell assembly.* S@Super P composite was mixed with the binder (PVDF) with a mass ratio of 9:1 in NMP by ball-milling for 1 h. After ball-milling, the as-obtained slurry was cast on an aluminum foil using a doctor blade and dried at 70 °C for 24 h in a vacuum oven. The electrode was cut in a circle ( $d = 12$  mm) and the actual amount of sulfur on each electrode was determined as 1.0 – 1.1 mg cm<sup>-2</sup>. The CR2032-type coin cell was fabricated using Li metal chip as a counter electrode, a separator (Celgard 2450), and an electrolyte (25  $\mu$ L cm<sup>-2</sup>) containing 1 M LiTFSI in a mixed solvent of 1,3-dioxolane and 1,2-dimethoxyethane (volume ratio = 1:1) with 1 wt.% LiNO<sub>3</sub> additive in a glovebox. To operate the flexible electrodes, Ni-deposited carbon fabric (NiCF) and Cu-deposited carbon fabric (CuCF) were used as cathode and anode supports, respectively. Li metal was deposited on the CuCF at 1 mA cm<sup>-2</sup> in 0 – 1 V

(Li<sup>+</sup>/Li) for five cycles to fabricate the Li/CuCF as an anode, while S@Super P was cast on the NiCF, which showed the S loading amount of 2.77 mg cm<sup>-2</sup> as a cathode. With the Li/CuCF anode and S@Super P/NiCF cathode, pouch cells were fabricated with the cathode size of 2 × 3 cm<sup>2</sup> to facilitate the curved electrodes. All procedures were performed under Ar atmosphere.

*Battery cell test.* Galvanostatic electrochemical impedance spectroscopy (GEIS) was performed on a PARSTAT MC (PMC1000/DC) electrochemical system (Princeton Applied Research, USA). The frequency range for the GEIS tests was from 10 mHz to 100 kHz with an amplitude current of 0.5 mA RMS (root mean square). Galvanostatic charge/discharge cycling tests were conducted on an WonATech battery testing system (WBCS3000L) at various current densities from 1.7 to 2.8 V (vs. Li/Li<sup>+</sup>). Cyclic voltammograms (CV) were measured from 1.7 to 2.8 V (vs. Li/Li<sup>+</sup>) at various scan rates from 0.1 to 0.5 mV s<sup>-1</sup>. All coin cells were tested after 24 h to allow the electrolyte to penetrate the cell.

*First-principles calculations.* DFT calculations were performed as implemented in the Vienna *ab initio* simulation package (VASP).<sup>[27]</sup> Generalized gradient approximations (GGA) were utilized to describe exchange-correlation (*xc*) functionals<sup>[28]</sup> and projector augmented wave (PAW) potentials<sup>[29]</sup> were applied for electron–ion interactions. Kinetic energy cut-off was set to 400 eV. For van der Waals (vdW) correction, we adopted the Grimme’s DFT-D3 scheme<sup>[30]</sup> based on a semi-empirical GGA-type theory. Computational model systems were constructed by RP chains and clusters, (15,0) zigzag CNT, and Li<sub>2</sub>S<sub>x</sub> (*x* = 1, 2, 4, 6, and 8). For the Brillouin-zone integration, (1 × 1 × 1) grid in the reciprocal space was used in the Gamma centered scheme. All atoms were fully relaxed until the Hellmann–Feynman forces and energies were converged within 0.02 eV/Å and 1 × 10<sup>-5</sup> eV, respectively.

## Supporting Information

Supporting Information (SI) is available from the Wiley Online Library or from the author.

SI includes TEM images with EDS mappings, Raman spectra, microscopic images, N<sub>2</sub> adsorption–desorption isotherms, pore size distributions, tensile strength–strain curves, XPS spectra, SEM images with EDS images, DFT calculations, and electrochemical tests.

## **Acknowledgements**

This work was supported by the Innovation and Technology Commission of Hong Kong, Research Institute for Smart Energy of the Hong Kong Polytechnic University (grant No. Q-CDA3), the National Research Foundation of Korea (NRF) grant funded by the Korea government (MSIT) (grant No. NRF-2020R1A2C2006720), and the Global Frontier Program through the Global Frontier Hybrid Interface Materials (GFHIM) of National Research Foundation of Korea (NRF) funded by the Ministry of Science and ICT (Project No. 2013M3A6B1078882).

Received: ((will be filled in by the editorial staff))

Revised: ((will be filled in by the editorial staff))

Published online: ((will be filled in by the editorial staff))



## Figures

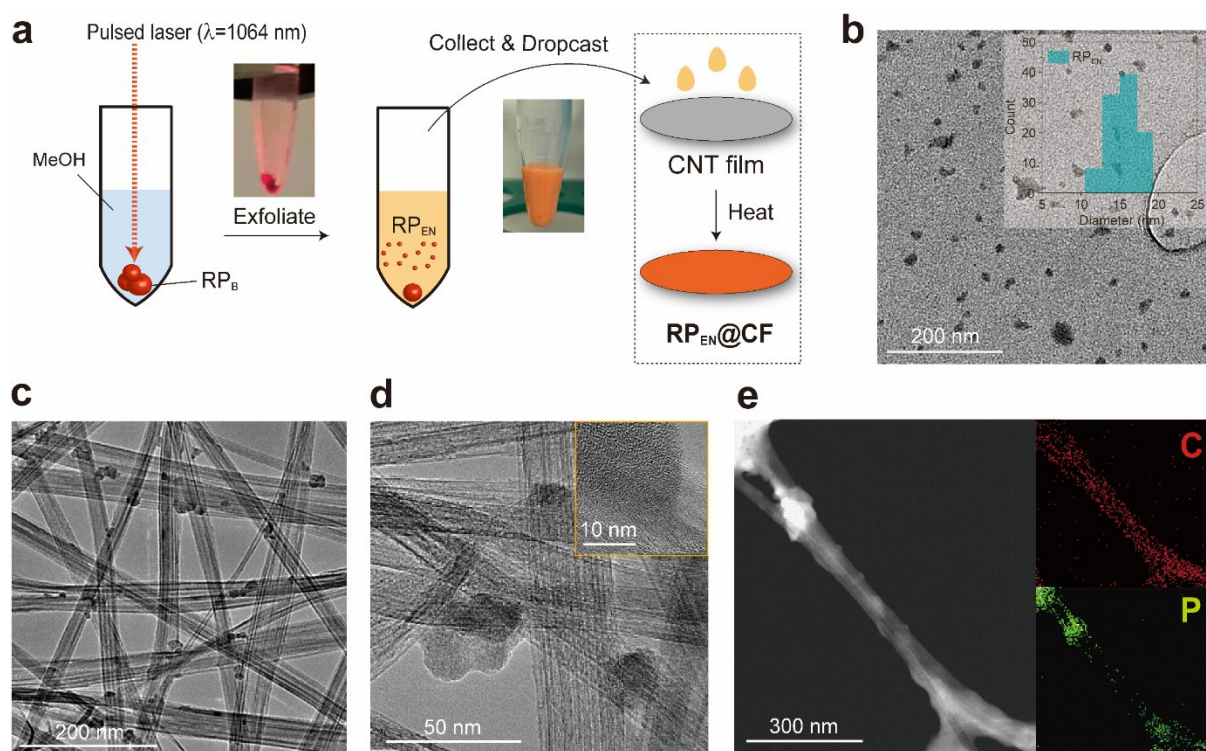


**Figure 1.** (a) Schematic illustration of the synthesis process for RP<sub>EN</sub>@CF interlayer. (b) TEM image of RP<sub>EN</sub> (inset: DLS analysis of RP<sub>EN</sub>). (c) TEM, (d) high-resolution TEM, and (e) EDS mapping images for C and P elements of RP<sub>EN</sub>@CF. Inset in (d) is the magnified region showing RP<sub>EN</sub>.

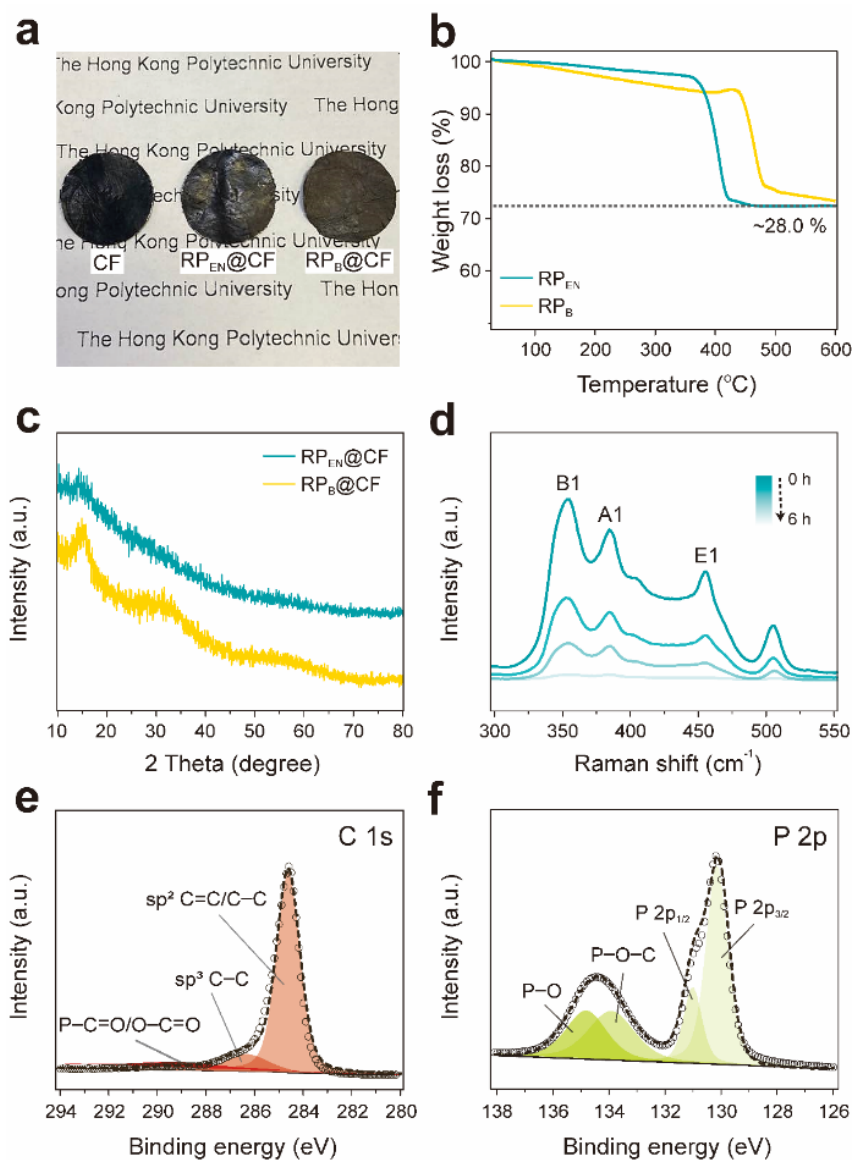


**Figure 2.** (a) Digital photographs of CNT film (CF), RP<sub>EN</sub>@CF, and RP<sub>B</sub>@CF. (b) TGA analysis in N<sub>2</sub> gas and (c) XRD patterns of RP<sub>EN</sub>@CF and RP<sub>B</sub>@CF. (d) Raman spectra of RP<sub>EN</sub> at various exposure times in air. XPS spectra of RP<sub>EN</sub>@CF in (e) C 1s and (f) P 2p regions.

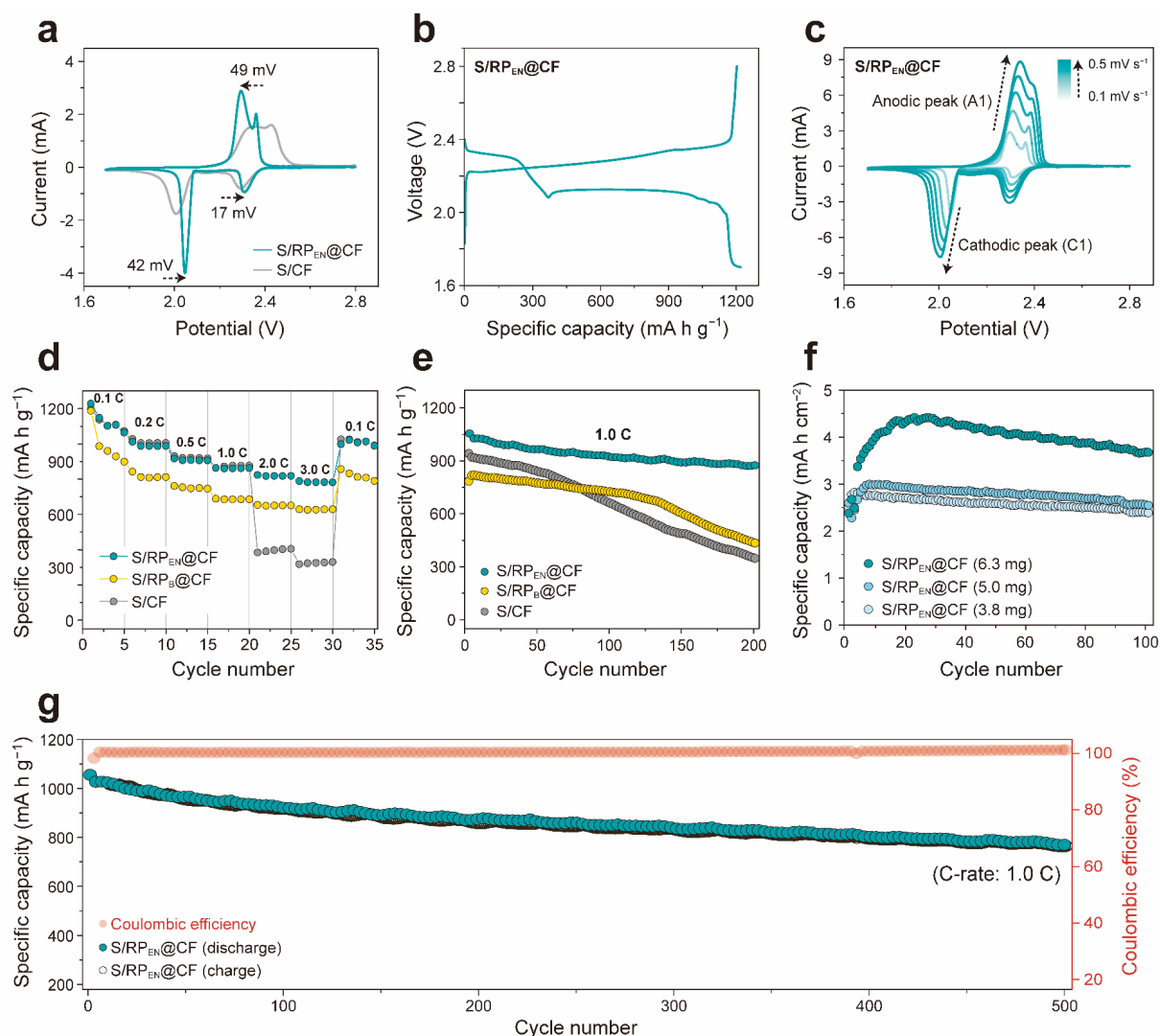


**Figure 3.** (a) CV curves of S/RP<sub>EN</sub>@CF and S/CF cells at the first cycle. (b) Galvanostatic discharge-charge profile of S/RP<sub>EN</sub>@CF cell at 1<sup>st</sup> cycle. (c) CV curve of S/RP<sub>EN</sub>@CF cell at various scan rates from 0.1 to 0.5 mV s<sup>-1</sup>. (d) Rate performance of S/RP<sub>EN</sub>@CF, S/RP<sub>B</sub>@CF, and S/CF cells. (e) Cycling performance of S/RP<sub>EN</sub>@CF, S/RP<sub>B</sub>@CF, and S/CF cells at 1.0 C for 200 cycles. (f) Cycling performance of S/RP<sub>EN</sub>@CF cells with S loading of 6.3, 5.0, and 3.8 mg for 100 cycles. (g) Long-term cycling performance of S/RP<sub>EN</sub>@CF cell at 1.0 C for 500 cycles.

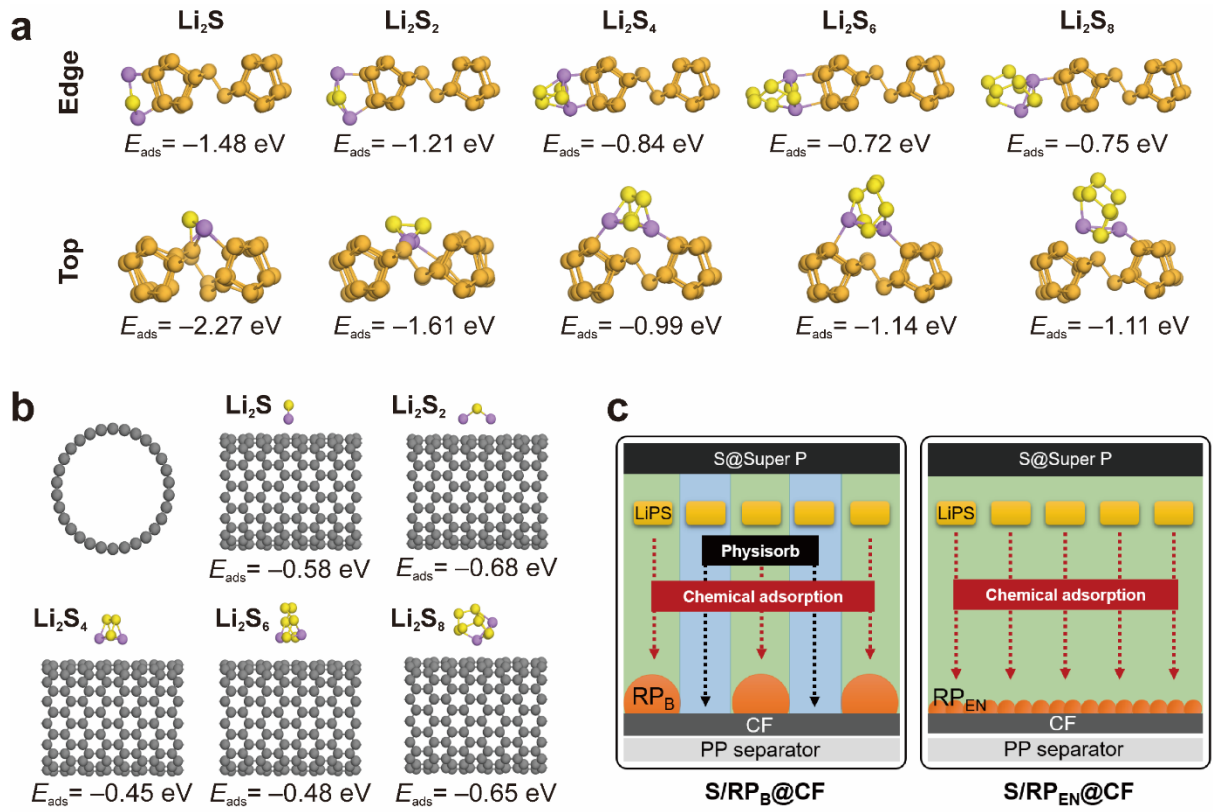


**Figure 4.** DFT calculations for adsorption energy ( $E_{\text{ads}}$ ) of LiPSs on (a)  $\text{RP}_\text{EN}$  and (b) CNT. Here, Li, S, P, and C atoms are colored by purple, yellow, orange, and gray, respectively. (c) Schematic illustrations of the immobilization of LiPSs by  $\text{S/RP}_\text{B}@\text{CF}$  and  $\text{S/RP}_\text{EN}@\text{CF}$ .

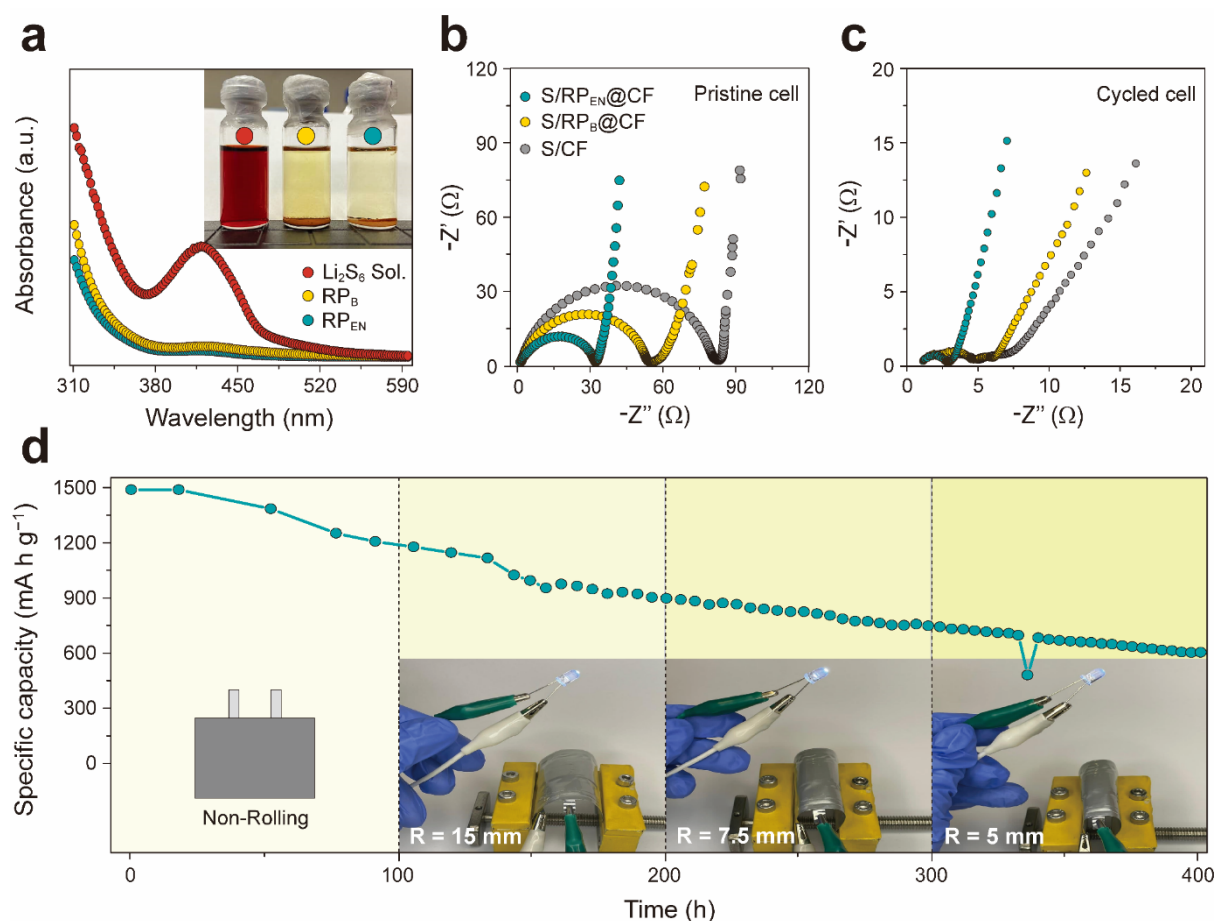


**Figure 5.** (a) UV-vis absorption spectra of 10 mM Li<sub>2</sub>S<sub>6</sub> solutions containing RP<sub>B</sub> and RP<sub>EN</sub>. Inset shows the digital photos of Li<sub>2</sub>S<sub>6</sub> solutions after 24 h of stirring. GEIS analysis of S/RP<sub>EN</sub>@CF, S/RP<sub>B</sub>@CF, and S/CF electrodes (b) before and (c) after 100 cycles. (d) Cycle performance of S/RP<sub>EN</sub>@CF full cell under mechanical roll-up.

## References

- [1] a) Z. W. Seh, Y. Sun, Q. Zhang, Y. Cui, *Chem. Soc. Rev.* **2016**, 45, 5605; b) N. S. Choi, Z. Chen, S. A. Freunberger, X. Ji, Y. K. Sun, K. Amine, G. Yushin, L. F. Nazar, J. Cho, P. G. Bruce, *Angew. Chem. Int. Ed.* **2012**, 51, 9994; c) P. G. Bruce, S. A. Freunberger, L. J. Hardwick, J.-M. Tarascon, *Nat. Mater.* **2011**, 11, 19.
- [2] a) B. Scrosati, J. Hassoun, Y.-K. Sun, *Energy Environ. Sci.* **2011**, 4, 3287; b) M. Armand, J. M. Tarascon, *Nature* **2008**, 451, 652; c) A. Manthiram, Y. Fu, Y. S. Su, *Acc. Chem. Res.* **2013**, 46, 1125.
- [3] a) Y. X. Yin, S. Xin, Y. G. Guo, L. J. Wan, *Angew. Chem. Int. Ed.* **2013**, 52, 13186; b) A. Manthiram, Y. Fu, S. H. Chung, C. Zu, Y. S. Su, *Chem. Rev.* **2014**, 114, 11751; c) W. Ahn, S. N. Lim, D. U. Lee, K.-B. Kim, Z. Chen, S.-H. Yeon, *J. Mater. Chem. A* **2015**, 3, 9461; d) X. Ji, K. T. Lee, L. F. Nazar, *Nat. Mater.* **2009**, 8, 500.
- [4] a) Y. Yang, G. Zheng, Y. Cui, *Chem. Soc. Rev.* **2013**, 42, 3018; b) Z. Li, Y. Huang, L. Yuan, Z. Hao, Y. Huang, *Carbon* **2015**, 92, 41.
- [5] a) J. He, Y. Chen, P. Li, F. Fu, Z. Wang, W. Zhang, *J. Mater. Chem. A* **2015**, 3, 18605; b) J. Lee, Y. Jeon, J. Oh, M. Kim, L. Y. S. Lee, Y. Piao, *J. Electroanal. Chem.* **2020**, 858, 113806.
- [6] a) K. Ding, Y. Bu, Q. Liu, T. Li, K. Meng, Y. Wang, *J. Mater. Chem. A* **2015**, 3, 8022; b) S. Liu, K. Xie, Z. Chen, Y. Li, X. Hong, J. Xu, L. Zhou, J. Yuan, C. Zheng, *J. Mater. Chem. A* **2015**, 3, 11395.
- [7] a) J. He, L. Luo, Y. Chen, A. Manthiram, *Adv. Mater.* **2017**, 29, 1702707; b) M. Kim, J. Lee, Y. Jeon, Y. Piao, *Nanoscale* **2019**, 11, 13758; c) X. Wang, G. Li, J. Li, Y. Zhang, A. Wook, A. Yu, Z. Chen, *Energy Environ. Sci.* **2016**, 9, 2533; d) S. S. Zhang, D. T. Tran, *J. Mater. Chem. A* **2016**, 4, 4371.
- [8] a) M. Chen, X. Wang, S. Cai, Z. Ma, P. Song, A. C. Fisher, *J. Mater. Chem. A* **2016**, 4, 16148; b) X. Zhao, H.-J. Ahn, K.-W. Kim, K.-K. Cho, J.-H. Ahn, *J. Phys. Chem. C* **2015**, 119, 7996.
- [9] a) Z. Li, C. Li, X. Ge, J. Ma, Z. Zhang, Q. Li, C. Wang, L. Yin, *Nano Energy* **2016**, 23, 15; b) Y. Tian, H. Huang, G. Liu, R. Bi, L. Zhang, *Chem. Commun.* **2019**, 55, 3243.
- [10] a) S.-H. Chung, A. Manthiram, *Joule* **2018**, 2, 710; b) J.-Q. Huang, Z.-L. Xu, S. Abouali, M. Akbari Garakani, J.-K. Kim, *Carbon* **2016**, 99, 624; c) Y. S. Su, A. Manthiram, *Chem. Commun.* **2012**, 48, 8817.
- [11] a) Y. Liu, X. Qin, S. Zhang, G. Liang, F. Kang, G. Chen, B. Li, *ACS Appl. Mater. Interfaces* **2018**, 10, 26264; b) Z. Xiao, Z. Yang, L. Wang, H. Nie, M. Zhong, Q. Lai, X. Xu, L. Zhang, S. Huang, *Adv. Mater.* **2015**, 27, 2891.
- [12] a) J. Yang, L. Yu, B. Zheng, N. Li, J. Xi, X. Qiu, *Adv. Sci.* **2020**, 7, 1903260; b) H. Lin, S. Zhang, T. Zhang, S. Cao, H. Ye, Q. Yao, G. W. Zheng, J. Y. Lee, *ACS Nano* **2019**, 13, 7073.
- [13] a) Y. Fan, Z. Yang, W. Hua, D. Liu, T. Tao, M. M. Rahman, W. Lei, S. Huang, Y. Chen, *Adv. Energy Mater.* **2017**, 7, 1602380; b) L. Qu, P. Liu, Y. Yi, T. Wang, P. Yang, X. Tian, M. Li, B. Yang, S. Dai, *ChemSusChem* **2019**, 12, 213.
- [14] a) Z. L. Xu, S. Lin, N. Onofrio, L. Zhou, F. Shi, W. Lu, K. Kang, Q. Zhang, S. P. Lau, *Nat. Commun.* **2018**, 9, 4164; b) J. Sun, Y. Sun, M. Pasta, G. Zhou, Y. Li, W. Liu, F. Xiong, Y. Cui, *Adv. Mater.* **2016**, 28, 9797.
- [15] Z. Wang, M. Feng, H. Sun, G. Li, Q. Fu, H. Li, J. Liu, L. Sun, A. Mauger, C. M. Julien, H. Xie, Z. Chen, *Nano Energy* **2019**, 59, 390.
- [16] a) Z. Ye, Y. Jiang, J. Qian, W. Li, T. Feng, L. Li, F. Wu, R. Chen, *Nano Energy* **2019**, 64, 103965; b) Y. Zhong, L. Yin, P. He, W. Liu, Z. Wu, H. Wang, *J. Am. Chem. Soc.* **2018**, 140, 1455.

- [17] H. Song, Y. Hwang, T. Kumar Vimal, Y. Jeong, *Carbon Lett.* **2018**, 27, 12.
- [18] K. A. Wepasnick, B. A. Smith, J. L. Bitter, D. Howard Fairbrother, *Anal. Bioanal. Chem.* **2010**, 396, 1003.
- [19] T. I. T. Okpalugo, P. Papakonstantinou, H. Murphy, J. McLaughlin, N. M. D. Brown, *Carbon* **2005**, 43, 153.
- [20] J. J. Niu, J. N. Wang, Y. Jiang, L. F. Su, J. Ma, *Micropor. Mesopor. Mater.* **2007**, 100, 1.
- [21] W. J. Li, S. L. Chou, J. Z. Wang, H. K. Liu, S. X. Dou, *Nano Lett.* **2013**, 13, 5480.
- [22] a) B. Peng, Y. Xu, K. Liu, X. Wang, F. M. Mulder, *ChemElectroChem* **2017**, 4, 2140; b) J. S. Li, Y. Wang, C. H. Liu, S. L. Li, Y. G. Wang, L. Z. Dong, Z. H. Dai, Y. F. Li, Y. Q. Lan, *Nat. Commun.* **2016**, 7, 11204.
- [23] a) Y. Wang, B. Yang, B. Wan, X. Xi, Z. Zeng, E. Liu, G. Wu, Z. Liu, W. Wang, *2D Mater.* **2016**, 3, 035025; b) W. Zheng, J. Lee, Z. W. Gao, Y. Li, S. Lin, S. P. Lau, L. Y. S. Lee, *Adv. Energy Mater.* **2020**, 10, 1903490.
- [24] a) J. Sun, H.-W. Lee, M. Pasta, Y. Sun, W. Liu, Y. Li, H. R. Lee, N. Liu, Y. Cui, *Energy Storage Mater.* **2016**, 4, 130; b) J. Sun, G. Zheng, H. W. Lee, N. Liu, H. Wang, H. Yao, W. Yang, Y. Cui, *Nano Lett.* **2014**, 14, 4573.
- [25] S.-K. Park, J. Lee, T. Hwang, Y. Piao, *J. Mater. Chem. A* **2017**, 5, 975.
- [26] Y.-T. Liu, D.-D. Han, L. Wang, G.-R. Li, S. Liu, X.-P. Gao, *Adv. Energy Mater.* **2019**, 9, 1803477.
- [27] a) G. Kresse, J. Furthmüller, *Phys. Rev. B* **1996**, 54, 11169; b) G. Kresse, J. Furthmüller, *Comp. Mater. Sci.* **1996**, 6, 15.
- [28] a) W. Kohn, L. J. Sham, *Phys. Rev.* **1965**, 140, A1133; b) J. P. Perdew, K. Burke, M. Ernzerhof, *Phys. Rev. Lett.* **1996**, 77, 3865.
- [29] P. E. Blöchl, *Phys. Rev. B* **1994**, 50, 17953.
- [30] S. Grimme, J. Antony, S. Ehrlich, H. Krieg, *J. Chem. Phys.* **2010**, 132, 154104.